Front. Earth Sci. 2024, 18(1): 68–82
https://doi.org/10.1007/s11707-022-1013-2

RESEARCH ARTICLE

Geochronology, petrogenesis, and geological significance of the quartz vein-type copper deposits in Longwei area, north-west Dayaoshan, Guangxi

Song FU[1], Shehong LI (✉)[2], Changxing LV[3], Longqing SHI[1], Xuhan HU[2], Jinming WU[2], Zhuolin XIE[2]

1 College of Earth Sciences & Engineering, Shandong University of Science and Technology, Qingdao 266590, China
2 School of Earth Sciences, Guilin University of Technology, Guilin 541006, China
3 Xinwen Mining Group Co., Ltd. Huafeng Coal Mine, Tai'an 271409, China

Abstract Quartz-vein-type copper deposits were discovered in SN-trend ore-bearing structures in north-west Dayaoshan, Guangxi. Lack of reports on the precise metallogenic age of these deposit has become a bottleneck in metallogenic research in this area. In this study, the quartz vein-type copper mine in Longwei area of Jinxiu was selected as the research object. Fresh illite samples in the fault gouges and ore samples were collected for testing and analysis. Based on the Re-Os isotope dating study, the age of pyrite isochron, belonging to the Caledonian period, was determined to be 417 ± 25 Ma, whereas that of chalcopyrite isochron belonging to the Indosinian period, was found to be 243 ± 18 Ma. Pyrite crystallized considerably earlier than chalcopyrite. The obtained EPMA data were combined with rock mineralogical analysis data, Metasomatous mineral pyrite and metasomatic mineral chalcopyrite were identified to have originated from different hydrothermal systems. In the Indosinian period, copper deposits in the Longwei area underwent pyrite crystallization, pyrite fragmentation, copper-bearing hydrothermal filling, and metasomatism, consolidating and forming minerals. The study determined the mineralisation time and ore sources of copper deposits in the Longwei area. The study provides evidence for the existence of Indosinian hydrothermal activities in the north-western Dayaoshan area.

Keywords Re-Os dating, electron probe, micro-analyser, quartz-vein copper deposit, Dayaoshan area

1 Introduction

Magmatic activities in Dayaoshan, Guangxi, have been significant during consecutive Caledonian, Hercynian-Indosinian, and Yanshan periods, which resulted in the formation of a large number of magmatic hydrothermal metal deposits in the region (Chen et al., 2015; Jiang et al., 2017; Dang et al., 2018). In the north-western region of Dayaoshan, which contains a large number of quartz vein-type metallic minerals, a few magmatic deposits have been discovered. However, the relationship between intrusive rock formation and mineralisation has been controversial to date. Some scholars believe that Caledonian magmatic activities and tectonic activities led to copper mineralisation in this area (Huang et al., 2003; Chen et al., 2015; Zhao et al., 2017). Some scholars believe that the frenetic germ layer formed in the Caledonian period, and mineralisation occurred in the Hercynian-Indosinian period (Luo, 2009; Xu et al., 2014; Lu et al., 2016), while some researchers believe that mineralisation occurred mainly due to the multistage magmatic activities from the Caledonian to the Yanshanian period (Deng, 2012). However, the precise age for the litholithic vein-type copper deposits in this area has not been determined so far. According to some dating models, the age of quartz vein-type metal deposits in the Early Paleozoic strata is close to or less than that of the surrounding rock strata (Luo, 2009; Deng, 2012; Xu et al., 2014). The north-western region of Dayaoshan contains three Caledonian acid granites, namely Dajin, Puquan, and Lingzu. Recent high-precision geochronological studies have reported that granitoid in this region was deposited during the early Paleozoic (430–470 Ma) (Li et al., 2016; Li et al., 2017; Chen et al., 2020), and the three granite bodies were formed before the formation of Devonian strata. These deposits are found in the Middle and Lower Devonian strata (354–410 Ma) in north-western Dayaoshan. Therefore, some scholars have asserted that the hydrothermal deposits were not affected

Received January 12, 2022; accepted May 9, 2022

E-mail: 837898471@qq.com

by the Caledonian magmatic activity in this area (Li et al., 2016).

Re-Os dating is the most commonly used method for quartz vein-type hydrothermal deposits (Chen et al., 2010; Huang et al., 2016), Among them, molybdenite dating is the fastest and most convenient method. Chalcopyrite and pyrite contain relatively less Re and Os, but the measured age of chalcopyrite and pyrite directly reflects the age of mineralisation, indicating that they have irreplaceable advantages (Deng et al., 2016). We investigated some mines but did not collect ore-related molybdenite from the north-western region of Dayaoshan. Chalcopyrite and pyrite were selected to explore the mineralisation time and material source in the Longwei area.

In this study, we determined and compared the geological features of Longwei Cu deposits and present Re-Os isochron age data, electronic probe data, and illite K-Ar dating for chalcopyrite and pyrite. This study aims to explore the nature of genetic processes involved in the formation of Longwei Cu deposits.

2 Geological background

Dayaoshan, Guangxi is located in the south-western part of the interface of the Yangtze and Cathaysia blocks (Fig. 1(a)). The exposed strata in the area mainly include Cambrian, Devonian, and Carboniferous. Caledonian and Yanshanian granite intrusions are also distributed in this region (Wang et al., 2013; Liu et al., 2021). The main structures in the area include the E-W-trending Dali deep fault and the Dayaoshan anticlinorium, which are further superimposed as NW-SE-, NE-SW-, and N-S-trending structures. Studies suggest that the main faults formed in the Caledonian period experienced multiple periods of tectonic activity (Deng, 2011; Wang et al., 2017).

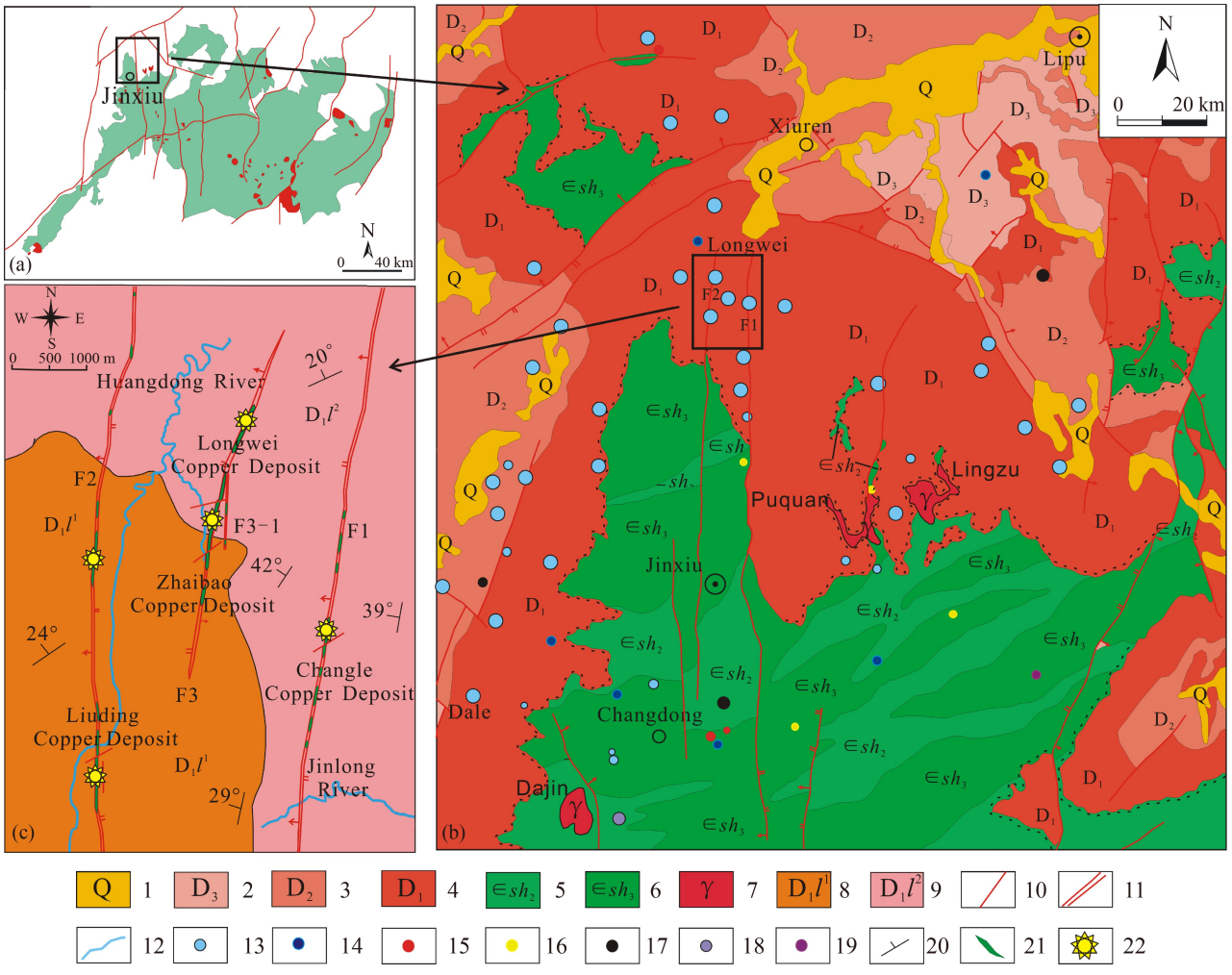

Fig. 1 Regional geological image. (a) Location image of the study area; (b) the regional geological image in north-western Dayaoshan of Guangxi; (c) the regional geological image of Longwei copper deposits. 1. Quaternary; 2. Upper of Devonian; 3. Middle of Devonian; 4. Lower of Devonian; 5. Middle of Cambrian Shuikou Group; 6. Upper of Cambrian Shuikou Group; 7. Acidic Granite; 8. Lower part of the Devonian Lianhuashan Formation; 9. Upper Lianhuashan Formation of Devonian; 10. Fault; 11. Fault zone; 12. River; 13. Copper Deposit; 14. Lead Deposit; 15. Gold Deposit; 16. Tin Deposit; 17. Leod-zinc Deposit; 18. Copper-lead-zinc Deposit; 19. Co-Ni Deposit; 20. Attitude; 21. Copper; 22. Sampling point.

The Cambrian Shuikou Group and Devonian strata are exposed in the north-west of Dayaoshan. The Devonian Lianhuashan Formation, Nagaoling Formation, and Donggangling Formation are the main strata characterized by quartz vein-type copper deposits (Fig. 1(b)). Only three granite bodies have been exposed in the north-western part of Dayaoshan. The lithology is granite and granite diorite, and the three granite bodies are in intrusive contact with the Cambrian strata. The Longwei area is concentrated in four deposits, that is, Longwei, Zhaibao, Liuding, and Changle. The similar features shared by these deposits including geological characteristics and genesis, spatial distribution of ore bodies, and ore structure composition were investigated in the present study.

The Longwei mining area is located between the Longwei and Huangjiatun regions in the north of Jinxiu County, north-west of Dayaoshan, Guangxi (Fig. 1(b)). Ore bodies are mainly found in three S-N-trending faults, namely F1, F2, and F3 (Fig. 1(c)). The Lower Devonian Lianhuashan Formation (D_1l) and Quaternary System are exposed in this area, which is in intrusive contact with the surrounding rock (Fig. 2(a)). The stratum has been affected by tectonic stress and hydrothermal alterations. Most rocks have been broken and have developed multiple sets of joints, with alterations seen along the fissures and bedding. Chalcopyrite is mostly irregular, with a particle diameter of approximately 0.05 mm, and it is symbiotically wrapped with quartz. Its symbiotic boundary is straight, indicating the characteristics of simultaneous formation (Fig. 2(b)). Pyrite cracks are filled with chalcopyrite, and large pyrite particles are wrapped with chalcopyrite. All pyrites are fragmented (Figs. 2(c) and 2(d)), indicating the characteristics of multistage mineralisation. Pyrite deposition may have been affected by structures and hydrothermal fluids, and thus, its Re-Os dating data may be not particularly reliable. Despite this, some studies have used the fragmented metasomatic structure of pyrite for Re-Os dating analyses to solve the problem of multistage metal mineral crystallization (Zhang et al., 2017; Zhao et al., 2019). In this study, pyrite and chalcopyrite from the same ore were used for Re-Os isotope dating experiments, and these data were combined with those of a comprehensive analysis of rock and mineral characteristics.

3 Sampling and analytical methods

3.1 Sampling

To determine the mineral source and mineralisation timing, we collected 13 fresh ore samples, including those of chalcopyrite, pyrite, bornite, chalcocite, and quartz, from three faults, F1, F2, and F3, in the Longwei ore field. The ore minerals mainly comprise chalcopyrite, pyrite, bornite, chalcocite, and quartz. Five chalcopyrite and pyrite samples from the vein were selected for Re-Os dating, and eight samples were used for analysis using the electron probe micro-analyzer (EPMA). A set of illite samples from fresh fault gouges was used for K-Ar dating.

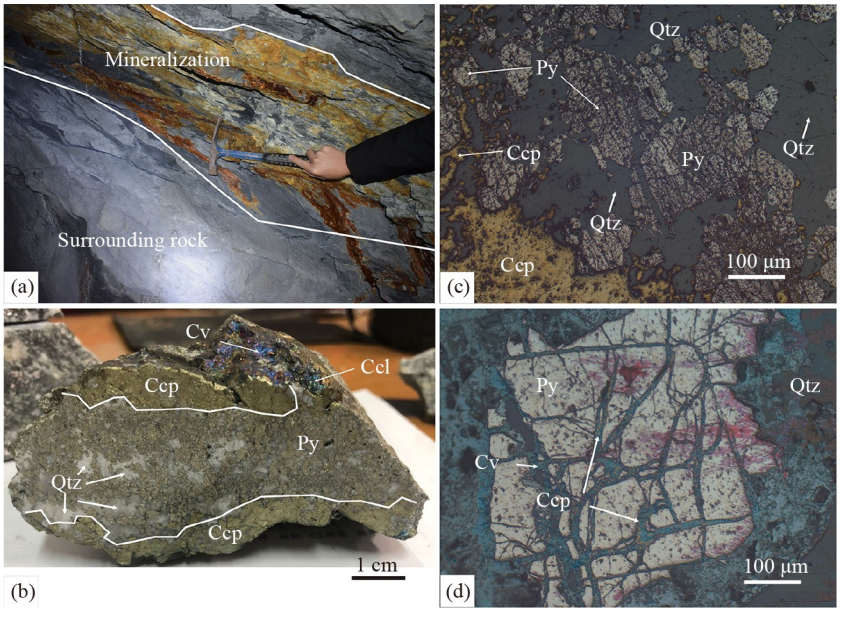

Fig. 2 Characteristic of minerals in quartz. (a) Characteristics of the intruder; (b) characteristics of ore sections; (c) fragmented pyrite (reflected light); (d) characteristics of chalcopyrite (reflected light). Py: Pyrite; Ccp: Chalcopyrite; Qtz: Quartz; Cv: Covellite; Ccl: Chrysocolla.

3.2 EPMA studies

Analysis using the EPMA was conducted in the Key Laboratory of the Guangxi Hidden Metallic Ore Deposits Exploration, Guilin University of Technology. EPMA studies were conducted on polished sections to determine the chemical composition of minerals by using a JXA-8230 electron microprobe equipped with a wavelength dispersive system. The measurement conditions were as follows: accelerating voltage = 20 kV, probe current = 15 nA, and beam diameter = 2 μm. Calibrations were performed using natural and synthetic reference materials such as forsterite (Mg, Fe, and Si), anorthite (Ca), albite (Na, Al), chromite (Cr), phlogopite (K), rutile (Ti), NiO, CoO, and MnO (Fu et al., 2018).

3.3 Chalcopyrite and pyrite Re-Os isotopic composition

The Re-Os isotope analyses were performed at the Guangzhou Institute of Geochemistry, Chinese Academy of Sciences, following the established procedures. Approximately 1–3 g of sample powder, comprising ^{190}Os (20 μL) and ^{185}Re (3–5 drops), and inverse aqua regia (HNO_3: HCl = 3:1, 10 mL) were frozen in a Carius tube, and the tube was sealed and heated at 240°C for 24 h. Os was extracted from the inverse aqua regia fraction through carbon tetrachloride solvent extraction and then back-extracted into concentrated HBr. Further purification was performed through micro-distillation by using chromic acid. Re was separated and purified from the remaining aqueous solution through anion exchange chromatography by using an AG1-X8 resin (100–200 mesh). Os isotopic compositions were measured through Triton thermal ionisation spectrometry, as described in the studies by Li et al. (2010, 2015a). Instrumental mass fractionation of Os was corrected by normalizing the measured $^{192}Os/^{188}Os$ ratio to 3.08271. Oxide corrections were made using the $^{17}O/^{16}O$ ratio of 0.00037 and $^{18}O/^{16}O$ ratio of 0.002047 (Li et al., 2015a). The $Os/^{188}Os$ ratio of the BHVO-2 standard is 0.1540 (550 ppt (parts per trillion) Re and 76 ppt Os; Li et al., 2015a), which is slightly higher than the $^{187}Os/^{188}Os$ value measured in the step of hydrofluoric acid desilicification during Carius Tube digestion (Li et al., 2015a).

3.4 Fault gouges illite K-Ar dating

K-Ar isotope dating was performed at the Analytical Laboratory of BRIUG. The samples were cleaned with alcohol, deionised water, and acetone through ultrasonic vibration and divided into two parts, and the absolute contents of $^{40}Ar^*$ and ^{40}K in the samples were determined. Briefly, for determining the $^{40}Ar^*$ content, an electronic balance (accuracy ± 0.001 mg) was used to accurately weigh a part of the sample, which was wrapped with pure aluminum foil for compaction. Then, the sample was placed in the injection turntable above the double vacuum heating furnace, and the injection turntable was vacuum-baked for 48 h to allow degassing to fully remove the gas adsorbed on the surface of the sample. Subsequently, the sample was transferred into a vacuum heating furnace to release the gas in the sample by using the full-melt method, and the gas was then allowed to pass through the liquid nitrogen U-type cold trap. After the gas was purified by two groups of zirconium–aluminum getter pumps (one at 450°C, and the other at room temperature), a certain amount of diluent ^{38}Ar was introduced; the gas released from the sample along with Ar and subsequently entered the Argus VI noble gas mass spectrometer, which facilitated analysis of the Ar isotopic composition. Based on the argon isotopic composition measurements and the amount of ^{38}Ar diluent, we calculated the absolute content of radiogenic $^{40}Ar^*$ in the sample. Similarly, for determining the ^{40}K content, an electronic balance (accuracy ± 0.001 mg) was used to accurately weigh another part of the sample, and its K content was determined through atomic absorption spectroscopy. Because the $^{40}K/K$ ratio in the earth lithosphere sample is constant, the measured K content was used to determine the ^{40}K content of the sample. The age of ^{40}K-^{40}Ar was calculated using the isotope system decay equation, in which the decay constant is calculated using 5.543×10^{-10} (Zhang et al., 2021).

4 Results

4.1 Electron probe micro-analyzer

EPMA data of pyrite and chalcopyrite from the Longwei Copper Mine are presented in Table 1 and Table 2, respectively.

Fe (43.98–46.94 wt.%) and S (51.16–53.76 wt.%) contents in pyrite were found to vary greatly. Twelve pieces (30%) of Fe/S were slightly larger than the theoretical value of 0.87, with an average ratio of 0.86. Other metal elements included Co, Pb, Mo, Ni and As, with average values of 0.13 wt.%, 0.02 wt.%, 0.93 wt.%, 0.04 wt.%, 0.12 wt.%, respectively. Overall, pyrite had a high content of As, Co, Ni, and Mo, and a low Zn content (0.01 wt.%).

Cu, Fe, and S contents in chalcopyrite were in the range of 33.65–36.17 wt.%, 28.31–31 wt.%, and 33.91–35.7 wt.%, respectively. The average contents of S and Fe (34.75 wt.% and 29.51 wt.%, respectively) were slightly lower than the theoretical values (34.92 wt.% and 30.52 wt.%, respectively), whereas the average content of Cu (34.66 wt.%) was slightly higher than the theoretical value (34.56 wt.%). The average value of Mo was 0.65 wt.%. Chalcopyrite exhibited an overall high Zn content and low As, Co, Ni, and Mo contents.

Table 1 EPMA analysis data of pyrite

Sample	As	Cu	Fe	Sb	Pb	Cd	Ni	Co	S	Zn	Te	Mo	Total/%	Ni/Co
G1-1-1	0.05	0.02	46.51	0.03	0.00	0.00	0.01	0.11	52.41	0.00	0.00	1.10	100.22	0.10
G1-1-2	0.07	0.26	45.20	0.00	0.02	0.00	0.01	0.06	52.90	0.02	0.00	0.85	99.38	0.11
G1-1-3	0.04	0.07	46.02	0.00	0.00	0.00	0.02	0.08	52.58	0.00	0.00	1.07	99.87	0.19
G1-1-4	0.03	0.02	44.34	0.02	0.00	0.04	0.02	0.09	53.72	0.00	0.03	1.20	99.47	0.17
G1-1-5	0.20	0.01	44.69	0.02	0.03	0.05	0.29	0.34	53.54	0.00	0.03	1.07	100.24	0.88
G1-1-6	0.00	0.22	44.46	0.00	0.00	0.03	0.01	0.11	53.16	0.02	0.02	1.07	99.09	0.10
G1-1-7	0.06	0.46	45.50	0.00	0.00	0.03	0.00	0.13	52.63	0.01	0.00	1.13	99.95	0.00
G1-1-8	0.01	0.12	45.91	0.02	0.00	0.01	0.01	0.08	52.37	0.02	0.00	1.12	99.65	0.14
G1-2-1	0.11	0.00	45.69	0.01	0.00	0.05	0.00	0.07	52.05	0.00	0.00	1.14	99.12	0.00
G1-2-2	0.09	0.08	45.76	0.00	0.01	0.09	0.03	0.17	52.94	0.02	0.00	1.09	100.28	0.15
G1-2-3	0.16	0.00	46.11	0.02	0.00	0.04	0.00	0.09	52.35	0.02	0.00	1.13	99.90	0.00
G1-2-4	0.14	0.08	45.00	0.04	0.00	0.02	0.00	0.22	51.78	0.01	0.03	1.11	98.41	0.00
G1-2-5	0.05	0.02	46.16	0.00	0.00	0.05	0.02	0.13	51.99	0.00	0.00	1.09	99.49	0.14
G1-2-6	0.39	0.84	45.19	0.04	0.00	0.00	0.02	0.11	53.36	0.00	0.00	0.95	100.90	0.39
G1-2-7	0.79	0.21	45.63	0.05	0.10	0.00	0.15	0.24	52.98	0.01	0.01	0.98	101.13	0.79
G1-2-8	0.00	0.02	46.29	0.00	0.00	0.06	0.01	0.08	54.12	0.00	0.00	1.00	101.57	0.00
G1-3-1	0.00	0.14	45.72	0.03	0.04	0.01	0.00	0.09	53.24	0.02	0.01	1.01	100.30	0.00
G1-3-2	0.01	0.00	46.08	0.00	0.00	0.02	0.02	0.24	53.47	0.00	0.00	1.02	100.85	0.01
G1-3-3	0.00	0.00	46.01	0.00	0.01	0.02	0.03	0.13	54.46	0.00	0.00	0.96	101.60	0.00
G1-3-4	0.39	0.84	45.19	0.04	0.00	0.00	0.02	0.11	53.36	0.00	0.00	0.95	100.90	0.39
G1-3-5	0.79	0.21	45.63	0.05	0.10	0.00	0.15	0.24	52.98	0.01	0.01	0.98	101.13	0.79
G1-3-6	0.02	5.11	44.19	0.00	0.14	0.01	0.02	0.08	52.39	0.00	0.00	0.02	101.97	0.02
G1-4-1	0.69	1.58	44.09	0.00	0.01	0.00	0.01	0.09	52.84	0.01	0.00	0.02	99.35	0.69
G1-4-2	0.00	1.57	46.83	0.00	0.09	0.00	0.17	0.09	51.16	0.00	0.00	0.00	99.91	0.00
G1-4-3	0.05	0.02	46.51	0.03	0.00	0.00	0.01	0.11	51.41	0.00	0.00	1.10	99.22	0.05
G1-4-4	0.07	0.26	44.20	0.00	0.02	0.00	0.01	0.06	53.90	0.02	0.00	0.85	99.38	0.07
G1-4-5	0.04	0.07	46.02	0.00	0.00	0.00	0.02	0.08	54.58	0.00	0.00	1.07	101.87	0.04
G1-4-6	0.03	0.02	44.34	0.02	0.00	0.04	0.02	0.09	53.72	0.00	0.03	1.20	99.49	0.03
G1-4-7	0.01	0.00	46.08	0.00	0.00	0.02	0.02	0.24	53.47	0.00	0.00	1.02	100.85	0.01
G1-4-8	0.00	0.00	46.01	0.00	0.01	0.02	0.03	0.13	54.46	0.00	0.00	0.96	101.60	0.00
G1-5-1	0.01	0.02	46.91	0.00	0.04	0.00	0.00	0.15	51.27	0.00	0.00	0.62	99.00	0.01
G1-5-2	0.00	0.00	45.98	0.01	0.00	0.00	0.01	0.16	53.14	0.01	0.00	1.10	100.42	0.00
G1-5-3	0.00	0.00	46.53	0.03	0.00	0.03	0.02	0.12	53.53	0.00	0.00	1.13	101.39	0.00
G1-5-4	0.00	0.02	45.46	0.00	0.00	0.03	0.04	0.19	53.65	0.00	0.00	1.09	100.48	0.00
G1-5-5	0.00	0.02	45.95	0.00	0.00	0.02	0.01	0.09	52.93	0.00	0.00	1.13	100.14	0.00
G1-5-6	0.00	0.00	45.52	0.01	0.00	0.05	0.01	0.10	53.68	0.00	0.00	1.04	100.41	0.00

Note: all the data are presented in wt.%.

4.2 Chalcopyrite and pyrite Re-Os isotopic composition

Tables 3 and 4 present the Re-Os isotopic compositions of chalcopyrite and pyrite from Longwei, respectively. Chalcopyrite from the Longwei vein-type ores comprised 13.87–318.41 ppt Re and 0.255–2.964 ppt Os, and its $^{187}Re/^{188}Os$ ratio ranged between 227.58 and 3313.98. All the five samples displayed the $^{187}Re/^{188}Os$ isochron age of 243 ± 18 Ma (MSWD = 0.45), with an initial $^{187}Os/^{188}Os$ ratio of 8.5 ± 0.624 (Fig. 3).

The pyrite samples separated from the Longwei vein-type ores have 115.16–262.9 ppt Re and 0.467–1.487 ppt Os, with $^{187}Re/^{188}Os$ ratios between 1082.95 and 6512.37. Re-Os isochron age of five pyrite samples is

Table 2 EPMA analysis data of the chalcopyrite

Sample	As	Cu	Fe	Sb	Pb	Cd	Ni	Co	S	Zn	Te	Mo	Total/%	Ni/Co
T1-1-1	0.02	35.16	30.03	0.01	0.00	0.05	0.01	0.04	34.69	0.01	0.00	0.66	100.64	0.13
T1-1-2	0.01	34.33	29.56	0.00	0.00	0.03	0.01	0.06	35.38	0.03	0.00	0.63	100.04	0.19
T1-1-3	0.00	33.96	30.56	0.02	0.00	0.05	0.01	0.08	35.14	0.03	0.03	0.68	100.55	0.16
T1-1-4	0.05	34.08	30.65	0.02	0.00	0.02	0.00	0.07	35.28	0.04	0.01	0.82	100.99	0.06
T1-1-5	0.00	33.65	29.82	0.00	0.00	0.03	0.00	0.05	34.98	0.04	0.00	0.73	99.31	0.04
T1-1-6	0.00	34.63	29.56	0.00	0.00	0.00	0.02	0.06	35.22	0.05	0.00	0.68	100.21	0.36
T1-1-7	0.00	34.48	29.66	0.00	0.07	0.00	0.00	0.06	34.80	0.04	0.00	0.69	99.80	0.03
T1-1-8	0.00	34.12	29.35	0.00	0.00	0.00	0.00	0.04	34.56	0.00	0.00	0.64	98.71	0.00
T1-2-1	0.02	34.21	29.23	0.00	0.00	0.03	0.01	0.04	33.91	0.05	0.00	0.64	98.12	0.34
T1-2-2	0.00	34.55	29.34	0.01	0.05	0.04	0.00	0.05	34.19	0.01	0.00	0.65	98.90	0.06
T1-2-3	0.00	36.17	28.90	0.00	0.01	0.03	0.01	0.06	34.38	0.02	0.00	0.71	100.29	0.18
T1-2-4	0.00	34.76	29.61	0.00	0.00	0.01	0.00	0.04	34.85	0.04	0.00	0.60	99.91	0.03
T1-2-5	0.00	34.75	29.78	0.01	0.10	0.00	0.00	0.04	34.60	0.04	0.00	0.76	100.09	0.00
T1-2-6	0.01	34.63	29.97	0.00	0.01	0.05	0.00	0.05	34.91	0.01	0.02	0.67	100.33	0.00
T1-2-7	0.00	34.64	29.81	0.02	0.00	0.03	0.00	0.04	34.90	0.00	0.00	0.72	100.16	0.00
T1-2-8	0.00	34.70	29.78	0.00	0.03	0.05	0.00	0.04	34.76	0.02	0.01	0.71	100.11	0.00
T1-3-1	0.00	34.43	28.52	0.00	0.03	0.02	0.00	0.06	34.41	0.04	0.00	0.66	98.16	0.00
T1-3-2	0.01	34.00	28.89	0.00	0.09	0.00	0.00	0.06	34.62	0.03	0.00	0.36	98.05	0.00
T1-3-3	0.00	35.01	29.37	0.00	0.07	0.03	0.00	0.06	34.34	0.05	0.00	0.25	99.18	0.00
T1-3-4	0.00	35.67	29.62	0.00	0.05	0.01	0.00	0.04	35.29	0.02	0.00	0.51	101.19	0.00
T1-3-5	0.00	35.10	29.89	0.00	0.00	0.03	0.00	0.05	34.44	0.04	0.00	0.60	100.16	0.00
T1-3-6	0.00	33.94	29.88	0.08	0.00	0.04	0.00	0.06	35.00	0.01	0.02	0.69	99.73	0.00
T1-3-7	0.00	34.49	31.00	0.01	0.04	0.05	0.01	0.08	34.59	0.01	0.00	0.52	100.80	0.12
T1-3-8	0.00	34.71	30.18	0.00	0.01	0.00	0.00	0.04	34.37	0.02	0.00	0.69	100.01	0.00
T1-4-1	0.00	34.19	28.63	0.00	0.08	0.02	0.00	0.05	34.63	0.02	0.00	0.72	98.34	0.00
T1-4-2	0.02	35.13	29.10	0.00	0.00	0.03	0.00	0.07	34.75	0.02	0.00	0.59	99.69	0.00
T1-4-3	0.02	34.69	29.56	0.00	0.05	0.00	0.00	0.06	34.88	0.06	0.00	0.73	100.03	0.00
T1-4-4	0.00	34.07	29.79	0.02	0.08	0.00	0.00	0.03	34.30	0.06	0.00	0.62	98.96	0.00
T1-4-5	0.00	34.85	29.73	0.00	0.00	0.04	0.00	0.05	35.24	0.00	0.00	0.67	100.56	0.00
T1-4-6	0.00	34.91	28.55	0.00	0.00	0.02	0.00	0.04	35.70	0.00	0.00	0.64	99.86	0.03
T1-4-7	0.00	35.65	28.31	0.01	0.09	0.03	0.00	0.05	35.09	0.07	0.00	0.61	99.90	0.00
T1-4-8	0.02	34.68	28.65	0.07	0.01	0.00	0.00	0.06	34.05	0.06	0.00	0.60	98.17	0.00
T1-5-1	0.00	34.63	29.04	0.00	0.08	0.00	0.00	0.07	34.32	0.00	0.00	0.61	98.75	0.00
T1-5-2	0.00	35.33	28.90	0.01	0.00	0.00	0.00	0.06	35.05	0.03	0.00	0.67	100.04	0.00

Note: all the data are presented in wt.%.

417 ± 25 Ma (MSWD = 0.92), with initial $^{187}Os/^{188}Os$ of 2.37 ± 0.68 (Fig. 4).

Re and Os contents in chalcopyrite and pyrite are low, because of which the isochronal age may not be precisely determined. Several studies have reported Re-Os dating data for chalcopyrite, pyrite, and pyrrhotite, and these data exhibit a large variation. For example, in sulphide ores in Dabaoshan, Guangdong, Re-Os isochron ages for pyrrhotite and chalcopyrite were determined to be 410 ± 16 Ma and 243 ± 41 Ma, respectively (Ying et al., 2017). In the Ashele copper-lead mine in Xinjiang, the Re-Os isochron age for chalcopyrite was determined to be 342 ± 11 Ma (Gao et al., 2019). The Re-Os isochron age for Dahongshan chalcopyrite was reported to be 1115 ± 28 Ma (Jin et al., 2017), whereas that for Tibet Dangxiong pyrrhotite was reported to be 309 ± 31 Ma (Cui et al., 2011). The values of 432 ± 23 Ma and 442 ± 17 Ma have been reported for pyrite in Tuolugou cobalt (gold) deposit in Qinghai (Feng et al., 2006) and that of 309 ± 31 Ma has been reported for pyrrhotite in the Lawu

Table 3 Re-Os isotope data for pyrite

Sample	Common Re		Common Os/ppt		$^{187}Re/^{188}Os$		$^{187}Os/^{188}Os$	
	Value/ppt	2σ	Value/ppt	2σ	Ratio	2σ	Ratio	2σ
TY-2	262.90	13.29	1.487	0.021	2851.01	149.62	18.12	0.24
TY-3	141.93	5.69	0.878	0.068	6512.37	470.08	41.54	0.51
TY-4	195.68	14.09	1.391	0.013	1185.33	86.05	5.88	0.08
TY-5	175.40	12.54	1.070	0.013	1082.95	66.66	5.12	0.06
TY-6	115.16	11.70	0.467	0.019	3589.15	392.49	21.61	0.26

Note: all the Re and Os blanks have low single-digit to sub-picogram level with a nonradiogenic Os isotopic composition.

Table 4 Re-Os isotope data for chalcopyrite

Sample	Re		Os		$^{187}Re/^{188}Os$		$^{187}Os/^{188}Os$	
	Conc/ppt	2σ	Conc/ppt	2σ	Ratio	2σ	Ratio	2σ
HY-2	195.07	11.27	1.792	0.015	1513.22	88.35	14.58	0.13
HY-3	44.24	5.26	0.255	0.025	3313.98	509.50	22.83	0.29
HY-4	23.87	6.90	1.118	0.011	227.58	65.83	9.42	0.09
HY-5	36.17	8.44	1.345	0.014	279.86	74.31	9.72	0.10
HY-6	318.41	21.96	2.964	0.057	573.53	81.08	10.96	0.14

Note: All the Re and Os blanks have all low single-digit to sub-picogram level with a nonradiogenic Os isotopic composition

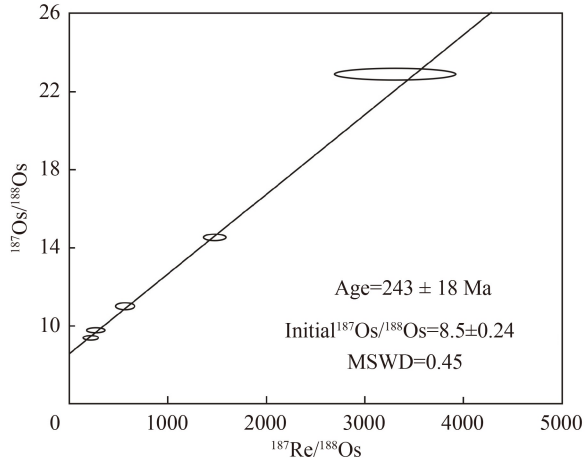

Fig. 3 Re-Os isochron line of pyrite.

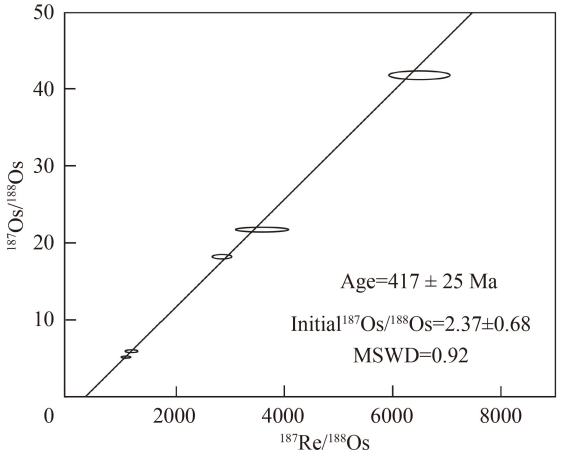

Fig. 4 Re-Os isochron line of chalcopyrite.

copper deposit in Tibet (Cui et al., 2011). Magmatic, tectonic, and hydrothermal activities in the Dayaoshan area have occurred during multiple periods, which impact the Re-Os isotope dating of chalcopyrite and pyrite, and thus, their Re-Os isochron age should not be deduced based only on data. Accordingly, the mineralisation laws of rock minerals and regional magma are discussed in this study.

4.3 Fault gouges illite K-Ar dating

The object of K-Ar dating was authigenic illite in clay. Therefore, in the first step, authigenic illite was separated from other clastic minerals. Theoretical and practical knowledge suggests that the separation of authigenic illite and detrital illite is achieved by grading (Zhang et al., 2007). From Table 5, it can be seen that the age of authigenic illite in the faults in the study area is 242.4 ± 5.1 Ma, which is higher than the age of the Devonian strata. Due to the small number of real samples, the K-Ar experiment was used for confirmation.

5 Discussion

5.1 Mineralogy and textures

5.1.1 Metasomatic structure of ore

Ore metasomatism refers to the direct effect of ore-

Table 5 Illite K-Ar data

Sample	Sample weighing/mg	K_2O/%	($^{40}Ar/^{38}Ar$)/m	($^{38}Ar/^{36}Ar$)/m	$^{40}Ar/(mol\cdot g^{-1})$	$^{40}K/(mol\cdot g^{-1})$	Age/(Ma,1σ)
YLS01	3.384	5.4	8.22	708.32	1.95×10^{-9}	1.29×10^{-7}	242.4 ± 5.1

Note: ($^{38}Ar/^{36}Ar$) measure.

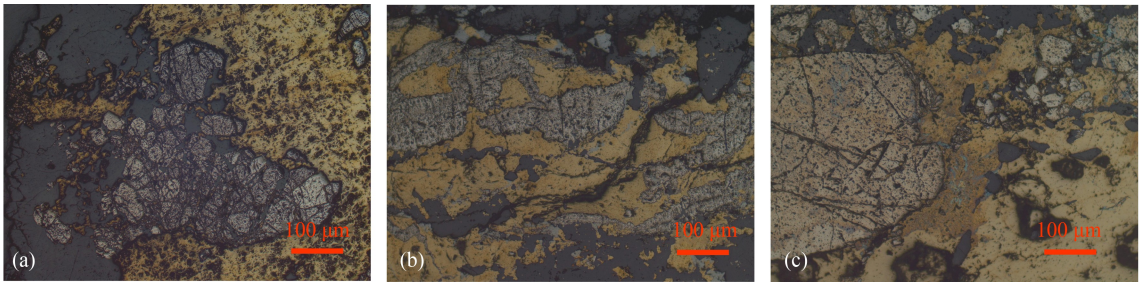

Fig. 5 Ore replacement structure. (a) Ore replacement structure of F1; (b) ore replacement structure of F2; (c) ore replacement structure of F3.

forming solutions on rocks or minerals (Hu et al., 2002). Crystallization of metasomatic minerals occurs in a sequence. However, it can occur during different stages of the same geological event or the superimposition of multiple geological events (Gu et al., 2004).

Both the quartz vein-type copper deposits in the study area and the north-western part of Dayaoshan developed metasomatic structures. The metabolised mineral was pyrite, and metasomatous pyrite was a copper-bearing ore-forming hydrothermal fluid (Fig. 5). These phenomena indicate that the deposits may have undergone the same ore formation process, indicating that the ore mineral analysis in the study area is aptly represented.

Studies have determined that pyrites are the minerals that have been replaced, along with small quartz fragments remaining on the edges of pyrite phenocrysts, which are fragmented and of varying sizes. The large pyrite particles retain the original euhedral or other crystal morphologies. Some mineral particles have straight edges and corners, and the fractured particles have become slightly rounded after metasomatic dissolution. The pyrite surface is uneven, and the holes are filled with weak sphalerite minerals.

In metasomatism pyrite, chalcopyrite and quartz show complete crystal morphologies and smooth surfaces. These two minerals are filled in the fractured pyrite fissures. Chalcopyrite is distributed chiefly in disseminated, metasomatic, and clumpy shapes. Chalcocite, bornite, sphalerite, galena, and pyrite crystallized at the same time as chalcopyrite did. Among these, chalcopyrite, bornite, and chalcocite in the shallow part were oxidised into covellite, whereas lead-zinc and iron minerals were oxidised on the surface into gossan.

The metasomatic ore structure indicated that fragmented pyrite formed before the crystallization of chalcopyrite, bornite, and chalcocite by the copper-bearing hydrothermal solution. A small amount of lead-zinc ore was observed in the edges of chalcopyrite and depressions of pyrite in the late crystallization period of chalcopyrite, a late crystalline mineral. The copper-bearing hydrothermal fluid is filled into fragmented pyrite. Chalcopyrite, chalcocite, bornite, and lead-zinc are crystallized. The copper ore in the deposit is formed through the late filling and metasomatism of copper-bearing hydrothermal fluid, which is condensed and crystallized.

5.1.2 Structure of the fragmented ore

Pyrite has a typical fragmentation structure. Similar to the metasomatic structure, pyrite fragmentation is widespread in the deposits in the Dayaoshan area (Fig. 6).

Pyrite exhibits three types of fragmentation. i) The fragmented particles are aggregated or scattered and of different sizes; these particles have angular and sub-angular structures, and their long axis is oriented in such a manner that they can show the direction of hydrothermal filling and flow (Fig. 6(c)). ii) The pyrite crystals are fragmented, but most of the crystal shape is retained. The ore-bearing hydrothermal fluid fills along the cracks of the fragmented crystal form (Fig. 6(a)). iii) The pyrite fragments are broken along a specific direction to form thin strips, which shows that the pyrite is fragmented along the direction of a specific force (Fig. 6(b)).

The fragmentation of metasomatic minerals in ore typically occurs through three routes. First, metasomatous minerals are broken or deformed under dynamic geological action, and this process occurs before metasomatism of ore-forming hydrothermal fluids. Second, early crystalline minerals are ‘heated’ or ‘degraded’ with an increase or decrease in the temperature of the ore-forming hydrothermal fluid, resulting in fragmentation. Finally, metasomatous and metasomatic minerals are degraded by the tectonic activity after mineralisation.

In the study area, only pyrite was broken, and chalco-

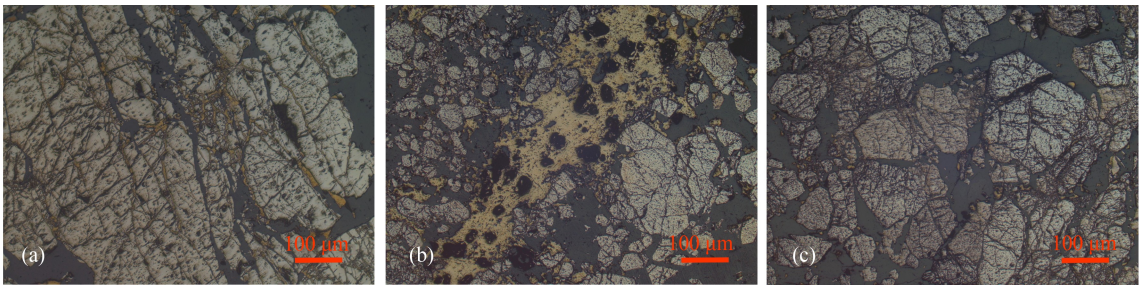

Fig. 6 Ore fragmentation structure. Py: Pyrite; Ccp: Chalcopyrite; Qtz: quartz.

pyrite and quartz did not exhibit specific degradation phenomena, indicating that the fragmentation of pyrite did not occur after mineralisation. Moreover, fragmented pyrite exhibited obvious migration and rotation characteristics, which shows that pyrite was crushed due to some geological event before the crystallization of chalcopyrite. The copper-bearing ore-forming hydrothermal fluid migrated and led to the transportation of fragmented pyrite. With changes in the temperature of the ore-forming hydrothermal fluid, the metasomatic minerals degraded. Mineral cracking is mainly caused by thermal expansion and contraction. Fissures are chiefly perpendicular and parallel to the mineral crystal boundary and mineral cleavage plane, respectively. Y- and T-type fissures are easily formed in the minerals. In the study area, there are a small number of similar fissures attributed to pyrite, but they are not the dominant type. The fragmentation of iron ore is mainly attributed to the change in the temperature of the ore-forming hydrothermal fluid.

With a decrease in the temperature of the same hydrothermal system, high-temperature minerals first crystallized and then formed cemented phenocrysts. The crystals exhibited euhedral and other forms, with a similar particle morphology, and phenocryst minerals were present in many combinations. Phenocrysts in the ore are mainly pyrite with extremely small amounts of other metals, and they have mixed particle sizes. Some phenocryst fractures comprise small amounts of Y- and T-type cracks; however, these cracks are related to fragmentation and are not formed during the ‘heating’ or ‘degradation’ process of hydrothermal temperature change. All the fragmented plaque, fragmented breccia, and crushed fabrics are the typical characteristics of a brittle dynamic action (Fig. 6(a)). Fragmented pyrite particle sizes range from a few nanometres to hundreds of nanometres, with particles that are mixed and have poor spherical morphologies and mainly angular and sub-angular shapes (Fig. 6(b)). Fragmented pyrite particle are mixed and have poor spherical morphologies and mainly angular and sub-angular shapes, with sizes ranging from a few nanometres to hundreds of nanometres (Fig. 6(b)). Under the action of the ore-forming hydrothermal fluid, fragmented pyrite is transported and migrated through osmotic metasomatism, leading to fragmentation and cataclastic flow (Figs. 6(b) and 6(c)). Pyrite fragmentation is terminated by the external dynamic geological action, which is consistent with the strip-shaped fragmentation of some pyrites, and granular pyrite may be transported across multiple periods or moved with the hydrothermal fluids.

Metasomatic and fragmentation structures of the ore indicate that ore formation occurred in at least three stages. In the first phase, metasomatous mineral pyrite crystallized. Crystallization conditions were relatively stable, leading to the formation of euhedral crystals or large particles. In the second phase, pyrite fragmented due to external dynamic geological action, which led to the formation of numerous channels in the rock and mineral. In the third stage, the copper-bearing hydrothermal fluid replaced fragmented pyrite, and through the condensation and crystallization of the ore-forming hydrothermal fluid, copper-bearing minerals and other metal minerals precipitated. Subsequently, near-surface minerals oxidised to produce altered metal minerals. Among these, metasomatism of the third stage ore-bearing hydrothermal fluid was the main mineralisation period.

5.2 Homology of metal minerals

Pyrite crystallizes first and is predominantly present in the ore. Studies have shown that Co, Ni, As, S, and Fe in pyrite can adequately represent the genesis of the deposit (Meng et al., 2002). Generally, Ni/Co > 1 indicates sedimentation; 0.2 < Ni/Co < 1 indicates magmatism; and Ni/Co < 0.2 indicates volcanic hydrothermal or contact metasomatism. According to the EPMA data, pyrite exhibited the Ni/Co ratio of 0.875 in one case and that of < 0.2 in other cases. In this ore, Ni/Co in pyrite varies considerably (0–1.857). Co-Ni in pyrite is mainly in the sedimentary and magmatic origin areas (Fig. 7).

The content of S/Fe in pyrite also provides source information (Zhou et al., 2005). Typically, the ratio of sedimentary genesis is close to the theoretical value or high sulfur content; the sulfur content in case of internal genesis is low. In this study, S/Fe in pyrite was between 0.825 and 0.888, which was > 46% greater than the theoretical value of 0.871. The data showed that pyrite is mainly of endogenous hydrothermal type, with added sedimentary materials.

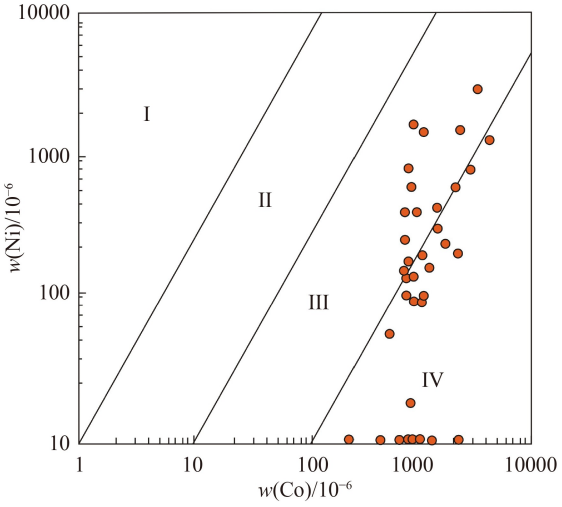

Fig. 7 Co/Ni distribution of pyrite in ore. I. Volcanic origin; II. hydrothermal origin; III. sedimentary genesis; IV. origin of Magma.

The Re-Os isotope system can effectively provide the ore deposits source (Stein et al., 2001). Re and Os exhibit fractionation in the mantle and crust; Re is a moderately incompatible element; thus, it can be easily transferred from the mantle to magma fluid. By contrast, Os is highly compatible with ore elements, and the separation of Os from the mantle is difficult. Therefore, the Re-Os isotope system is an indicator of the degree of incorporation of crustal materials during mineralisation (Li et al., 2011).

In the Re-Os dating experiment, the initial value of $(^{187}Os)/(^{188}Os)$ is 2.37 ± 0.68 in pyrite, which is considerably higher than that in mantle Os (0.12 to 0.13) and lower than that in the average continental crust (3.63) (Xu et al., 2019). The initial values for pyrite in the Longwei area indicate that pyrite was derived from a mixture of crustal materials and mantle input.

To verify whether copper ore and pyrite originated from the same hydrothermal system, we analyzed and compared their mineral geochemical characteristics.

In hydrothermal copper deposits, trace elements of metallic minerals aided the identification of the source area (Zhao et al., 2018). A comparison of elemental contents between chalcopyrite and pyrite showed that pyrite and chalcopyrite have a similar Pb content, whereas the content of other trace elements differed considerably between phenocryst pyrite and matrix chalcopyrite (Fig. 8). In addition, As, Mo, and Co tend to be more concentrated in pyrite than in chalcopyrite. Zn and Ni were dispersed in chalcopyrite pyrite. As Mo can easily enter pyrite, it effortlessly enters chalcopyrite. The average Mo content in chalcopyrite in the study area is 0.65%, which is smaller than that in pyrite (0.933%). Most pyrite had Pb/Zn > 1 and 1 < Co/Ni < 5, whereas most chalcopyrite had Pb/Zn < 1 and Co/Ni > 5.

The difference in the content of trace elements between

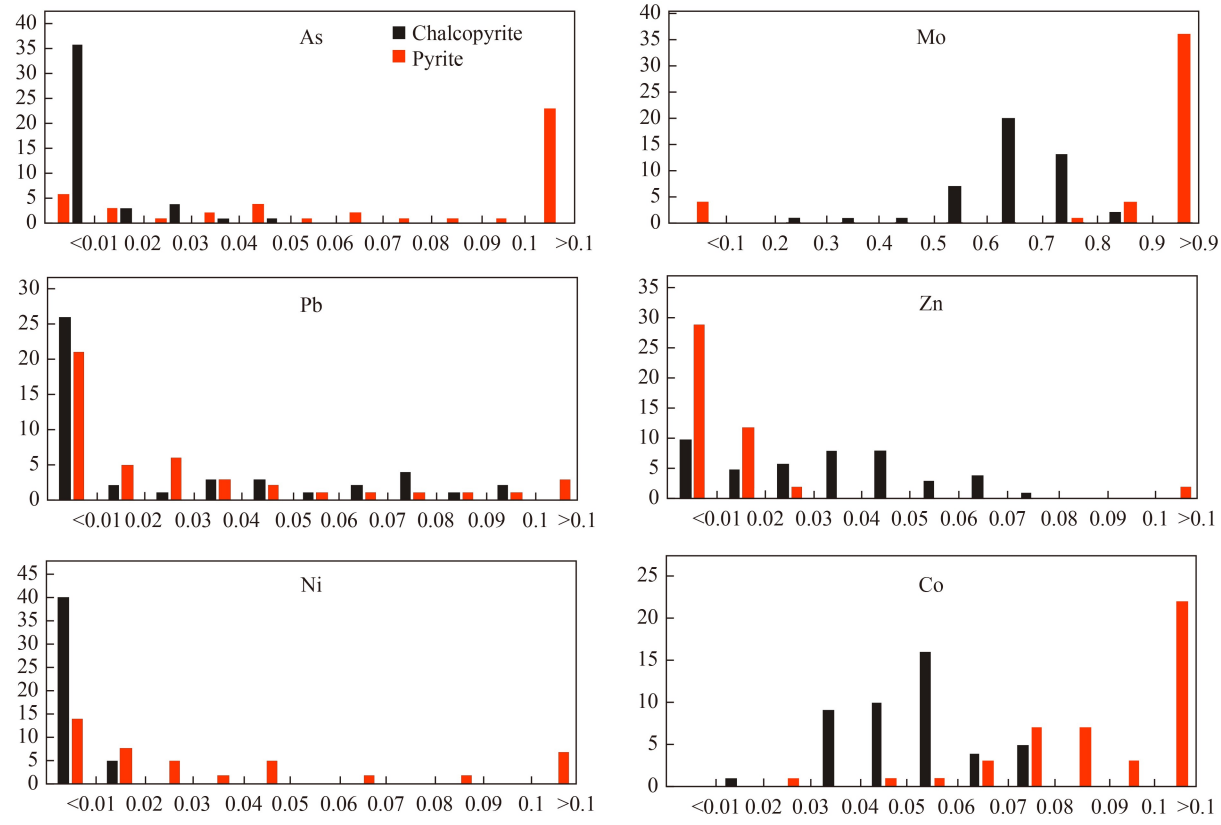

Fig. 8 Distribution spectrum of main trace metal elements in pyrite and chalcopyrite.

chalcopyrite and pyrite indicated that their sources are different and that they originate from hydrothermal systems having different properties. This result is consistent with the metasomatic structural characteristics of the ore.

The Re-Os isotope system is an effective tracer for sulphide mineralisation (Mao et al., 2001). According to the copper and iron properties of Re, the abundance value of Re exhibited an upward trend from the crust to core. A comprehensive analysis of the Re content of Mo in various deposits in China revealed that from the mantle to crust source, the Re content gradually decreased by an order of magnitude (Mao et al., 2003). However, more data are required to determine whether chalcopyrite is the same as Mo.

According to the Re-Os experimental data reported in studies by Stein et al. (2001) and Arne et al. (2001), sulphides are derived from shells: low Os and high n(^{187}Re)/n(^{188}Os); measured data of chalcopyrite: Os is 0.255–2.964; (^{187}Re)/(^{188}Os) is 228–3314. The initial value of chalcopyrite in the Re-Os experiment was (^{187}Os)/(^{188}Os) = 8.5 ± 0.24, which was higher than that in the average continental crust (3.63) (Xu et al., 2019). It has obvious characteristics of crust origin, and chalcopyrite-forming minerals mainly come from the stratum.

5.3 Pyrite crystallization time

The Re-Os isochron age of pyrite, which belongs to the Caledonian period, was determined to be 417 ± 25 Ma. Because the superposition of late-stage structure and hydrothermal fluids affects pyrite, studies should investigate whether a pyrite crystallization event occurred in the Caledonian period by using geological and mineralisation factors. The Caledonian granitoid activity is chiefly distributed at the junction of the Cathaysia Block and Yangtze Craton (Chen et al., 2012; Li et al., 2017). Researchers have reported that this tectonic effect is a key contributor that caused large-scale metal mineralisation in the Indosinian and Yanshanian periods in south China (Li et al., 2015b).

Many Caledonian acid intrusive rocks and related gold, molybdenum, and copper deposits developed in the southern part of Dayaoshan (Chen et al., 2011, 2012; Wang et al., 2013; Zhang et al., 2014; Liu et al., 2021). However, the dating data for the Caledonian deposit in the north-west of Dayaoshan are lacking. Although predecessors have concluded that the Caledonian period was a porphyry-skarn-quartzite vein-type tungsten-molybdenum-copper ore-forming period (Chen et al., 2015), representing the first activity period of ore-bearing hydrothermal fluids in multiphase mineralisation (Deng, 2011). However, only a few studies have reported the age of ore deposits and exact years. Luo (2009) reported the age of the Pb isotopic patterns of galena in sulphide ores of copper-lead-zinc deposits in north-western Guangxi as: three pieces of 429–452 Ma, nine pieces of 329–378 Ma, and one piece of 202 Ma. The Longhua Ni-Co deposit occurs in the N-E-trending fault near the Dajin granite body, and the Re-Os age of Ni-Co deposits was accurately determined to be 462.6 ± 8.5 Ma (Huang et al., 2020). Lead-zinc mineralised quartz veins exist in Dajin rock, and the hydrothermal activity time obtained by mica Ar-Ar dating is 399.3 ± 3.6 Ma (Liu et al., 2021). The age data of pyrite obtained in this study provides a basis for determining the crystallization age of pyrite.

Caledonian movements in south China can be divided into: the South China Ocean subducted Yunkai Block of 460–440 Ma, and collision and extension stages of the Yangtze plate and Yunkai block of 440–400 Ma (Liu et al., 2018). The ages of Dajin, Puquan, and Lingzu magmatic rocks are concentrated in the 414–446 Ma range. Geochemical analyses suggest that these are type I or A with added mantle material, which offers suitable material conditions for sulphide crystallization (Li et al., 2016; Li et al., 2017; Chen et al., 2020). According to the EPMA data of pyrite and the Co/Ni distribution map, pyrite exhibits the formation characteristics and magma of common origin. The initial value (2.37 ± 0.68) of the pyrite Re-Os in the experiment is considerably higher than that in the mantle (1.2 to 1.3) and lower than that in average continental crust (3.63) (Chen et al., 2011). The aforementioned analysis suggests that pyrite crystals formed probably by the action of magma on the strata under the tensional environment after the late Caledonian collision, although this assumption requires further verification.

5.4 Chalcopyrite crystallization time

The Re-Os isochron age of chalcopyrite, which belongs to the early Indosinian period, is 243 ± 18 Ma. A few studies have reported Indosinian magma and deposits in the Dayaoshan area. However, based on the structure and mineralisation laws, some scholars have stated that the Indosinian period had the mineralisation potential (Luo, 2009; Deng, 2012). According to the 1:50000 and 1:200,000 geological maps, the S-N-trending fault was formed in the Late Devonian-Middle Triassic. The S-N-trending fault cuts through the Cambrian, Devonian, and Early Middle Carboniferous strata, and it is covered with the Triassic strata. The paleo-stress field and structure analyses suggest that the regional compression in the NW-SE direction influenced the strata in the Late Permian-Middle Triassic, which caused the S-N-direction ore-hosting fault to strike-slip to the left (Wang et al., 2017). Fault gouge was collected from the ore-bearing fault, and illite of 1-μm grain size was selected, which could not be dated using the Ar-Ar method. Thereafter, a

duplicate sample was used for K-Ar dating, and the age was determined to be 242.4 ± 5.1 Ma, similar to the chalcopyrite age (Table 5). We consider that the ore-bearing fault moved during the Indosinian period, and the copper-bearing hydrothermal fluid filling along the fault occurred simultaneously.

Numerous 240–260 Ma magmatic rocks exist in the Shiwandashan-Darongshan area in southern Guangxi (Wang et al., 2016; Wang et al., 2018). The north-east region extends through the southern Dayaoshan. This is evident in the 243–264.4 Ma granite and felsic dykes in the Renhe-Nanan and Longtoushan area (Deng, 2011; Duan et al., 2011; Chen et al., 2015). Many acid dykes invaded along the fault from the Xiangzhou to Wuxuan area on the west side of the Dayao Mountain. The K-Ar gain of the entire rock is 243.8 Ma. K-Ar dating was used for the lamprophyre vein (257 Ma) in the Malian area located in south of the study area (Deng, 2011; Chen et al., 2015). The traces of Indosinian magma and hydrothermal activity can be observed in the north-western region of Dayaoshan. Due to the large thickness of Paleozoic Devonian and Carboniferous strata, the exposure is less in this region. Geophysics confirmed the existence of a large concealed rock mass in the deep north-west of the Dayao Mountain (Luo, 2009).

The initial $^{187}Os/^{188}Os$ value of chalcopyrite was 8.5 ± 0.24, which was close to that of Proterozoic metamorphic sedimentary rocks (9.68) (Xu et al., 2019). This indicates that the brass mineral source is related to the deep ancient sedimentary base. Rock geochemistry has shown that acidic magmatic rocks in the Darongshan area that formed during this period are a product of remelting of crust-derived materials in Proterozoic rocks (Wang et al., 2016; Wang et al., 2018). Therefore, the formation of copper-bearing hydrothermal fluids in the Longwei Copper Mine is assumed to be related to hidden magma and hydrothermal activities in the Indosinian period.

In this study, the crystallization age of chalcopyrite was found to be 243 ± 18 Ma, which determined the mineralisation age of quartz vein-type copper deposits in Longwei area. This mineralisation age is reported for the first time and confirms the existence of the Indosinian hydrothermal activity in the north-western region of Dayaoshan.

5.5 Deposit origin

The pyrite and chalcopyrite dating data showed that in the Longwei area, ore formation of the copper deposits started from the Caledonian pyrite crystallization until the Indosinian period, in which the main copper-bearing mineral crystals were filled. In the north-west of the Dayao Mountain, Caledonian magma and ore-bearing hydrothermal activities can be observed, with trace amounts of lead, zinc, and other minerals. Quartz vein-type Ni-Co-Cu ore bodies formed in the faults of the Cambrian strata (Li et al., 2017; Huang et al., 2020). During the Caledonian period, the study area exhibited a post-collision extensional environment. This environment facilitated the separation of metal elements from the stratum and magma through ore-bearing hydrothermal fluids for the first enrichment (Liu et al., 2018). However, the age of pyrite (417 ± 25 Ma) obtained in this study must be verified in future studies.

The development of shear cracks, transcrystalline cracks, and fragmentation flow in pyrite indicated that pyrite was broken with external forces. During the Indosinian period, the studied strata were squeezed in the N-W direction, resulting in the fragmentation of the Cambrian, Devonian, and Carboniferous strata (Wang et al., 2017). Simultaneously, the re-movement of S-N-trending provided space for hydrothermal filling.

With ore-bearing fault activation, the copper-bearing hydrothermal fluid penetrated along the ore-bearing fault, and the fault was filled with metasomatic fragmented pyrite. Chalcopyrite crystallized at 243 ± 18 Ma to form the ore. Since then, the ore body has not been subjected to a high stress, and chalcopyrite and quartz crystal forms have remained intact. Currently, the exploration depth of ore bodies in the Longwei area is limited. The temperature of the collected 60 inclusions is concentrated in the range of 108°C–256°C, which is the same as the temperature of inclusions in this area (Luo, 2009).

According to a comprehensive analysis, the formation of quartz vein-type copper deposits in the north-western region of Dayaoshan may be related to the magmatic and hydrothermal activities during Caledonian and Indosinian periods. The findings of this study provide Re-Os dating data to support this assumption, although more robust evidence is needed.

5.6 Mineralisation age of Longwei mining area

Quartz vein-type copper deposits in the Dayaoshan area are controlled through S-N-trending faults. In general, typical fragmentation and metasomatic structures are developed. Studies have shown that several structurally controlled hydrothermal copper deposits are exposed. The main mechanism is the formation of buoyancy-driven magma rise (Saein and Afzal, 2017). This study showed that ore crystallization underwent three stages: pyrite crystallization, pyrite fragmentation, and copper-bearing hydrothermal filling.

Re-Os isotope data indicated the age of pyrite as 417 ± 25 Ma, which represents late Caledonian period. The geochemical analysis of pyrite showed mineral crystallization to be related to the formation and magmatism and the addition of deep mantle material. This finding is similar to the results of acid intrusive rocks in the north-western part of Dayaoshan (446–419 Ma). They have the

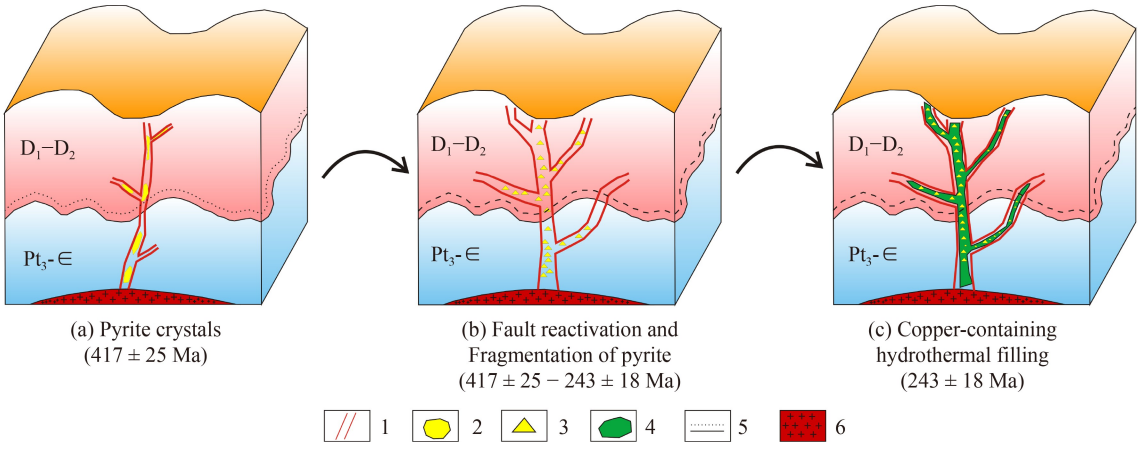

Fig. 9 Sketch map of metallogenic model.

1. Fault; 2. Pyrite; 3. Broken pyrite; 4. Copper hydrothermal; 5. Unconformity contact; 6. Concealed magmatic rock

characteristics of crust-mantle mixing (Xu et al., 2015). The age of hydrothermal quartz veins (399.3 ± 3.6 Ma) containing lead and zinc in Dajin rock is similar. The magma mixed with mantle material is assumed to be intruded in the stratum and have formed the Caledonian (446–419 Ma) magmatic rock mass. At this time, the magma was initially controlled by the embryonic S-N-trending fault. For example, the Puquan and Zuling plutons are distributed in the S-N-trending faults and are generally distributed in S-N-trending bands. With magmatism, hydrothermal fluids containing metals such as Fe, Pb, and Zn were filled in the S-N-trending faults during the Caledonian period, and some of these entered the rock mass to form ore-bearing veins. The hydrothermal fluid filled in the S-N-trending fault crystallized pyrite, eventually causing mineralisation.

When the Caledonian movement ended, the Dayaoshan area continued to deposit, leading to the formation of thick Devonian Carboniferous littoral-neritic clastic rocks and carbonate deposits in the north.

The S-N-trending fault was reactivated in the Indosinian period. Multiple active faults led to the fragmentation of early crystallized pyrite, which was carried, filled, and metasomatised to form the quartz vein-type copper ore with the penetration of the copper-bearing hydrothermal fluid. Due to differences in the fault connectivity, the variations in the mineralisation of the same fault at different locations led to the formation of deposits, including the Longwei Copper Mine in the north-western region of Dayaoshan. The hydrothermal fluid penetrated sandstone at the bake fault edge to produce the bake edge, which led to the formation of fractured rock joints and caused the fissures to be cut off by the veins. This study explored the control conditions, geological characteristics, mineralogy, and geochemistry of the Longwei copper deposit. Based on the aforementioned analysis, a metallogenic model was established (Fig. 9).

6 Conclusions

The nature of genetic processes involved in the formation of copper deposits in the Longwei area was determined in this study. Based on the results and discussion, the following conclusions were drawn.

1) Pyrite and chalcopyrite originated from two hydrothermal systems with different properties.

2) The crystallization times of pyrite and chalcopyrite, determined according to Re-Os isotope dating, are 417 ± 25 and 243 ± 18 Ma, respectively.

3) The Longwei mining area is a modified, superimposed hydrothermal deposit. During the Caledonian magma and hydrothermal process, pyrite was crystallized in the S-N-hosting fault. This fault was broken due to the brittle structures to produce fragmented pyrite plaques. After generation of the Lower Devonian Lianhuashan Formation, the copper-bearing hydrothermal fluids were poured into the fragmented pyrite faults. Metasomatic filling led to the formation of modified, superimposed hydrothermal copper deposits.

Acknowledgments Mine staffs are thanked for their assistance during fieldwork. This study was financially supported by the Natural Science Foundation of Shandong Province (Nos. ZR2020KE023 and ZR2021MD057), the National Natural Science Foundation of China (Grant No. 42002282).

References

Arne D C, Bierlin F P, Morgan J W, Stein H J (2001). Re-Os dating of sulfides associated with gold mineralization in Central Victoria, Australia. Econ Geol, 96(6): 1455–1459

Chen H, Kang Z Q, Wu J C, Li D X, Cao Y, Wei T W, Wei N S, Liu D, Zhou T, Liu D M, Lan H Y (2020). Geochronology, genesis and geological significance of the Puquan granite in the Dayaoshan Area, Guangxi. Geoscience, 34(06): 1277–1290 (in Chinese)

Chen M H, Guo Y Q, Liang B, Huang H W (2012). Emplaced and

metallogenetic ages of Wujie tungsten and molybdenum occurrence and geochemical characteristics of granodiorite in Cangwu. J Guilin U Technol, 32(01): 1–13 (in Chinese)

Chen M H, Li Z Y, Li Q, Wei Z R, Huang H W, Zhang Z Q, Xiao L Y (2015). A Preliminary study of multi-stage granitoids and related metallogenic series in Dayaoshan area of Guangxi, China. Earth Sci Front, 22(2): 41–53

Chen W, Wan Y S, Li H Q, Zhang Z Q, Dai T M, Shi Z E, Sun J B (2011). Isotope geochronology: technique and application. Acta Geol Sin, 85(11): 1917–1947

Chen X H, Qu W J, Han S Q, Eleonora S, Yang N, Chen Z G, Zeng F G, Du A D, Wang Z H (2010). Re-Os geochronology of Cu and W-Mo deposits in the Balkhash metallogenic belt, Kazakhstan and its geological significance. Geosci Front, 1(1): 115–124

Cui Y B, Zhao Y Y, Qu W J, Liu W, Ye R, Liu Y (2011). Re-Os dating and ore-forming material tracing of the Lawu ore deposit in Damxung area, Tibet. Geol Bull China, 30(8): 1283–1293 (in Chinese)

Dang Y, Chen M H, Fu B, Mao J W, Fanning M C, Li Z Y (2018). Petrogenesis of the Yupo W-bearing and Dali Mo-bearing granitoids in the Dayaoshan area, south China: constraints of geochronology and geochemistry. Ore Geol Rev, 92: 643–655

Deng J (2011). Genesis of the copper-gold polymetallic deposits in Dayaoshan of Guangxi, China. Geo Resour, 20(4): 287–297 (in Chinese)

Deng J (2012). Metallogenic series and model of copper and gold polymetallic deposits in Dayaoshan, Eastern Guangxi. Geo Resour, 21(6): 552–556 (in Chinese)

Deng X H, Wang J B, Pirajno F, Wang Y W, Li Y C, Li C, Zhou L M, Chen Y J (2016). Re-Os dating of chalcopyrite from selected mineral deposits in the Kalatag district in the eastern Tianshan Orogen, China. Ore Geol Rev, 77: 72–81

Duan R C, Ling W L, Li Q, Chen Z W, Yang H M, Liu L F (2011). Correlations of the Late Yangshanian tectonomagmatic events with Metallogenesis in south China: geochemical constraints from the Longtoushan gold ore deposit of the Dayaoshan area, Guangxi Province. Acta Geol Sin, 85(10): 1644–1658

Feng C Y, Zhang D Q, Qu W J, Du A D, Li D X, She H Q (2006). Re-Os isotopic dating of pyrite in the Tuolugou SEDEX Cobalt (Gold) Deposit, Golmud, Qinghai Province. Acta Geol, 80(4): 571–576

Fu W, Zhang Y M, Pang C J, Zeng X W, Huang X R, Yang M L, Shao Y, Lin H (2018). Garnierite mineralization from a serpentinite-derived lateritic regolith, Sulawesi Island, Indonesia: mineralogy, geochemistry and link to hydrologic flow regime. J Geochem Explor, 188: 240–256

Gao L L, Wang K Y, Chen C, Zhang X B, Li J (2019). Tectonic setting and metallogenic chronology of the Ashele Cu-Zn of deposit in Xinjiang, NW China: constraints from Re-Os dating of pyrite, U-Pb dating of zircon and Hf isotopes. Ore Geol Rev, 115: 103163

Gu L X, Tang X Q, Zheng Y C, Wu C Z, Tian Z M, Lu X J, Ni P (2004). Deformation,metamorphism and ore-component remobilization of the Archaean massive sulphide deposit at Hongtoushan, Liaoning Province. Acta Petrol Sin, 4: 923–934

Hu S X, Zhao Y, Sun J G, Ling H F, Ye Y, Lu B, Ji H Z, Xu B, Liu H Y, Fang C G (2002). Fluids and Their sources for gold mineralizations in the north China Platform. J Nanjing U (Nat Sci), 3: 381–391 (in Chinese)

Huang H M, He Z J, Cui B (2003). Metallogenic series of granite in Dayaoshan of Guangxi. Geol Prospect, 39(4): 12–16 (in Chinese)

Huang W T, Wu J, Liang H Y, Chen X L, Zhang J, Ren L (2020). Geology, geochemistry and genesis of the Longhua low-temperature hydrothermal Ni-Co arsenide deposit in sedimentary rocks, Guangxi, South China. Ore Geol Rev, 120: 103393

Huang X W, Qi L, Gao J F, Meng Y M (2016). Some thoughts on sulfide Re-Os isotope dating. Bull Mine Petrol Geochem, 35(3): 432–440 (in Chinese)

Jiang X Z, Kang Z Q, Xu J F, Feng Z H, Pang C J, Fang G C, Wu J C, Xiong S Q (2017). Early paleozoic granodioritic plutons in the Shedong W-Mo ore district, Guangxi, southern China: products of re-melting of middle Proterozoic crust due to magma underplating. J Asian Earth Sci, 141: 59–73

Jin Y F, Li Y G, Fei G C, Zhou H, Sha X B, Feng Y C, Wu H (2017). Re-Os Isotopic dating of chalcopyrite in quartz vein from Dahongshan IOCG Deposit in Kangdian copper metallogenic belt and its significance. Acta Mine Sin, 37(04): 417–426 (in Chinese)

Li H, Liu Y H, Li Z, Zhou S F, Li X, Wei J Z (2016). Geochemical characteristics and geological significance of granite geochronology in Dayao mountain guangxi. J East China U Techn (Nat Sci), 39(1): 29–37 (in Chinese)

Li J, Xu J F, Suzuki K, He B, Xu Y G, Ren Z Y (2010). Os, Nd and Sr isotope and trace element geochemistry of the Mulipicrites: insights into the mantle source of the Emeishan Large Igneous Province. Lithos, 119(1–2): 108–122

Li J, Zhao P, Liu J J, Wang X C, Yang A W, Wang G Q, Xu J F (2015a). Reassessment of hydrofluoric acid desilicification in the carius tube digestion technique for Re-Os isotopic determination in geological samples. Geostand Geoanal Res, 39(1): 17–30

Li J, Zhong L F, Tu X L, Hu G Q, Sun Y M, Liang X R, Xu J F (2011). Platinum group elements and Re-Os isotope analyses for geological samples using a single digestion procedure. Geochimica, 40(4): 372–380 (in Chinese)

Li X F, Yu Y, Wang C Z (2017). Caledonian granitoids in the Jinxiu area, Guangxi, South China: implications for their tectonic setting. Lithos, 272–273: 249–260

Li X W, Li J, Bader T, Mo X X, Scheltens M, Chen Z Y, Xu J F, Yu X H, Huang X F (2015b). Evidence for crustal contamination in intra-continental OIB-like basalts from West Qinling, central China: a Re-Os perspestive. J Asian Earth Sci, 98: 436–445

Liu P F, Zhang J L, Wu Z Q, Zhang Q W, Wen M L, Luo X R, Zheng C J, Huang W B (2021). A geochronological and geochemical study on the granodiorite porphyry and its implication for the mineralization in the Dayaoshan metallogenic belt, southeastern China. Acta Geochim, 40(1): 106–122

Liu S F, Peng S B, Kusky T, Polat A, Han Q S (2018). Origin and tectonic implications of an Early Paleozoic (460–440 Ma) subduction-accretion shear zone in the northwestern Yunkai Domain, south China. Lithos, 322: 104–128

Luo Y E (2009). Ore-control factors and genesis of deposits in Cu, Pb, Zn polymetal ore belt in west of Dayaoshan, Guangxi autonomous region. Contributions to Geo Min Resourc Res, 24(1): 56–72 (in

Chinese)

Mao J W, Du A D, Seltmann R, Yu J J (2003). Re-Os ages for the Shameika porphyry Mo deposit and the Lipovy Log rare metal pegmatite, central Urals, Russia. Miner Depos, 38(2): 251–257

Mao J W, Zhang G D, Du A D (2001). Geology, Geochemistry, and Re-Os isotopic dating of the Huangjiawan Ni-Mo-PGE deposit, Zunyi, Guizhou Province-withe a discussion of the polymetallic mineralization of basal cambrian black shales in south China. Acta Geol Sin, 2: 234–243

Meng Y F, Zhai Y S, Cui B (2002). Typomorphic characteristics of Cambrian pyritein Dayaoshan-Xidamingshan, Guangxi, China. Mineral Deposits, 21(S): 900–912

Saein L D, Afzal P (2017). Correlation between Mo mineralization and faults using geostatistical and fractal modeling in porphyry deposits of Kerman Magmatic Belt, SE Iran. J Geochem Explor, 181: 333–343

Stein H J, Markey R J, Morgan J W, Hannah L, Scherstén A (2001). The remarkable Re-Os chronometer in molybdenite: how and why it works. Terra Nova, 13(6): 479–486

Stein H J, Morgan J W, Schersten A (2000). Re-Os dating of Low-level highly radiogenic (LLHR) sulfides: the Harnas gold deposit, southwest Sweden, records continental-scale tectonic events. Econ Geol, 95(8): 1657–1671

Wang G M, Huang C X, Wei Z R, Yang T, Ye Y L, Wang C J, Yang H C, Feng Y J, Guan X Y, Yan Y L (2017). Spatial and temporal distribution of metal deposits in Dali area, Guangxi, south China. Geo Mine Resour South China, 33(1): 47–64 (in Chinese)

Wang L, Long W G, Zhou D, Xu W C, Jin X B (2016). Late Triassic zircon U-Pb ages and Sr-Nd-Hf isotopes of Darongshan granites in southesatern Guangxi and their geological implications. Geol Bull China, 35(8): 1291–1303 (in Chinese)

Wang W B, Li J H, Xin Y J, Sun H S, Yu Y Q (2018). Zircon LA-ICP-MS U-Pb datingand geochemical analysis of the Darongshan-Shiwandashan granitoids in sourthwestern South China and their geological implications. Acta Geosci Sin, 39(2): 179–188 (in Chinese)

Wang X Y, Liu M Z, Zhou G F, Huang X Q, Wang R H (2013). A correlation study of Au-Polymetallic mineralization and granite-porphyry magmatism in the Xinping mining area of the Dayaoshan metallogenic belt, eastern Guangxi. Geoscience, 3: 585–592 (in Chinese)

Xu D M, Lin Z Y, Luo X Q, Zhang K, Zhang X H, Huang H (2015). Metallogenetic series of major metallic deposits in the Qinzhou-Hangzhou metallogenic belt. Earth Sci Front, 22: 7–24

Xu H, Cui Y L, Zhang M H, Rong H F, Liang T X, Yang F M (2014). The ore prospect directions and EH4 electromagnetic sounding evidence of Dale copper polymetallic deposit in Guangxi. Sci Techn Engin, 14(30): 1–7 (in Chinese)

Xu Y L, Huang D Z, Liu Z, Zhen T, Zhou W J (2019). Re-Os isotopic dating of pyrite from the Washan iron deposit in Ningwu Basin and its geological implications. Acta Petrol Miner, 38(02): 219–229 (in Chinese)

Ying L J, Wang D H, Li C,Wang K, Wang K J, Wang L G, Wang Y W,Zhang X, Jiang J C (2017). Re-Os dating of sulfides in the north stratiform ore body in Dabaoshan, Guangdong Province and its indication. Earth Sci Front, 24(5): 31–38

Zhang G Z, Xue C J, Chi G X, Liu J Y, Zhao X B, Zu B, Zhao Y (2017). Multiple-stage mineralization in the Sawayaerdun orogenic gold deposit, western Tianshan, Xinjiang: constraints from paragenesis, EPMA analyses, Re-Os dating of pyrite (arsenopyrite) and U-Pb dating of zircon from the host rocks. Ore Geol Rev, 81: 326–341

Zhang J, Liu H B, Li J J, Jin G S, Han J, Zhang J F, Shi X (2021). Determination of experimental parameters during measurement of 40 Ar content in K-Ar dilution method. Rock Mineral Analysis, 40(3): 451–459 (in Chinese)

Zhang Y, Chen K L, Liu X Y (2007). Study on the K-Ar dating of diagenetic illite in sedimentary rock samples-question and discussion. Rock Mineral Analysis, 26(2): 117–120

Zhang Z Q, Chen M H, Mo J W, Xiao L Y, Huang Z Z, Luo J, Qu C H (2014). Evolution and source tracing of the Shedong quartz vein type scheelite-molybdenite polymetallic deposit in Cangwu County, Guangxi. Acta Petrol Sin, 30(1): 281–291

Zhao L T, Wang J B, Wang Y W, Zhu X Y, Li C (2019). Pyrite Re-Os geochronology of the Sareke sediment-hosted Cu deposit, Xinjiang, NW China. Ore Geol Rev, 104: 620–627

Zhao Y L, Zhang Q W, Hu R G, Sun T, Liu R H, Huang J H, Lu J, Su F D (2017). 3D modeling and analysis of ore-controlling factors of Daiwu gold deposit in Dayaoshan Metallogenetic belt, eastern Guangxi. Mine Resour Geo, 31(2): 408–413 (in Chinese)

Zhao Y, Li N B, Jiang Y H, Niu H, Yang W B (2018). Multi-stage Cu remobilization of the Huping metamorphic-hydrothermal deposit in the southern North China Craton. Ore Geol Rev, 101: 870–884

Zhou X W, Li S R, Lu L, Lin W B (2005). Reserch on the composition typomorphism of pyrite from Longkeng gold-silver mineralization district in Wuyi, Zhejiang Province, China. Bull Mine Petrol Geochem, 24(4): 317–326 (in Chinese)